Electronic Supplementary Information

Experimental Section

Materials: Ethanol, ammonia, tetraethyl orthosilicate (TEOS), cerium (IV) sulfate $(Ce(SO_4)_2)$ resorcinol, formaldehyde, hydrofluoric acid, and ethylenediamine (EDA) were readily available and purchased from Aladdin Ltd. (Shanghai, China). Isopropyl alcohol (IPA) and potassium hydroxide (KOH) were purchased from Beijing Chemical Corporation. (Beijng, China). Nafion solution (5% w/w) was obtained from Sigma-Aldrich Chemical Reagent Co. Ltd. Ultrapure water (18.25 Ω) used throughout all experiments was purified through a Millipore system. All the reagents are of analytical grade and were used as purchased without further purification.

Catalyst synthesis: Typically, 4.8 ml of ammonia aqueous solution (28 wt%) was added to a mixture of deionized water (16.5 mL) and ethanol (113.4 mL), after 10 min vigorous stirring, 5 ml TEOS was added and stirring continued for 10 min. Subsequently, 0.32 g resorcinol, 0.46 ml formaldehyde and 0.1 mL EDA were added to the stirred solution. Then, the mixture was vigorously stirred for 18 h and transferred to 200 mL of Teflon-lined autoclave (100 ℃) for another 24 h. The brown products were obtained by centrifugation and dried at 80 ℃ for 12 h. Finally, the solid samples were carbonized by heating at 750 ℃ for 2 h under an Ar gas (99.999%) environment in a tube furnace, the SiO_2 templates were removed by treating the material in dilute HF solution overnight, and the control samples NHCSs-x ("x" denotes the EDA amount, x = 0.05, 0.15) were prepared with different amounts of EDA. HCSs were prepared in the same way except without EDA.

Characterization: XRD patterns were acquired on a Shimadzu XRD-6100 diffractometer with Cu Kα radiation (40 kV, 30 mA) of wavelength 0.154 nm (Japan). SEM images were collected on a GeminiSEM 300 scanning electron microscope (ZEISS, Germany) at an accelerating voltage of 10 kV. XPS measurements were performed on an ESCALABMK II X-ray photoelectron spectrometer using Mg as the exciting source. Raman spectroscopy measurements were performed on a Renishaw 1000 Raman imaging microscope system with an excitation wavelength of 632.8 nm.

TEM images were collected on a FEI Tecnai G2 F20 SWIN transmission electron microscope operated at 200 kV.

Electrochemical measurements: All the electrochemical experiments were performed on an electrochemical workstation (CHI 760E) in a three-electrode system. For the rotating ring-disk electrode (RRDE) measurements, a glassy carbon electrode with a diameter of 5.6 mm (0.246 cm^2), a Hg/HgO (1 M KOH filling solution) electrode and a platinum plate electrode (1 × 1 cm^2) were employed as working electrode, reference electrode, and counter electrode, respectively. The potentials reported in this experiment were converted to reversible hydrogen electrode (RHE) scale via normalization processing with the following equation: E (vs. RHE) = E (vs. Hg/HgO) + 0.059 × pH + 0.098 V. The RRDE was polished with different particle size of alumina powder (1 μm and 0.05μm) for 5 min and ultra-sonicated in ultrapure water for 10 s. The ink was prepared by mixing the catalysts in ultrapure water, IPA (v/v = 4/1) to achieve a catalyst concentration of 3 mg mL^{-1} with 20 μL Nafion solution via sonication for 30 min. Working electrode was obtained through spin-coating 5 μl of the catalytic ink onto the glassy carbon electrode (disk area: 0.246 cm^2; ring area: 0.186 cm^2) after natural drying. Before the linear sweep voltammetry (LSV) tests, cyclic voltammetry (CV) was performed in N_2-saturated 0.1 M KOH at a scan rate of 50 mV s^{-1} for around 20 cycles, in which a steady CV response was obtained. Pt ring was then electrochemically cleaned in the same potential range at a scan rate of 500 mV s^{-1} for 10 cycles. O_2 gas was purged into the electrolyte for 5 min (caution: if the time interval between the Pt ring cleaning and ORR measurement is long, the H_2O_2 selectivity can be underestimated due to the surface passivation of the Pt ring). The H_2O_2 production activity was assessed by LSV in O_2-saturated 0.1 M KOH electrolyte at a scan rate of 10 mV s^{-1} and a rotation speed of 1600 rpm. During the LSV testing, the Pt ring potential was fixed at 1.2 V versus. RHE. The H_2O_2 selectivity was calculated using the following relation:

$$H_2O_2(\%)= 200 \times I_{ring}/N/(I_{disk} + I_{ring}/N)$$

where I_{ring} is the ring current, I_{disk} is the disk current and N is the collection efficiency (0.35 after calibration).

The electron transferred number of per oxygen molecule in the ORR can be calculated by the Koutechy-Levich (K-L) equation (1).

$$1/J = 1/J_k + B^{-1}\omega^{-1/2} \qquad (1)$$

Where J_k is the kinetic current density and ω is the rotation rate. The value of B could be calculated from the slope of Levich equation (2) as follows:

$$B = 0.2nF(D_0)^{2/3}\upsilon^{-1/6}C_0 \qquad (2)$$

Where n is the electron transfer number of per oxygen molecule, F is the Faraday constant (F = 96485 C mol^{-1}), C_0 is the bulk concentration of O_2 (1.2×10^{-1} mol cm^3), D_0 is the diffusion coefficient of O_2 in 0.1 M KOH (1.9×10^{-5} cm^2 s^{-1}), υ is the kinetic viscosity (0.01 cm^2 s^{-1}), the constant is 0.2 when the rotation speed unit is represented as rpm.

The electrogeneration of H_2O_2: The electro-generation of H_2O_2 was evaluated in a two-compartment cell with Nafion membrane as separator. First, the membrane was protonated by in 5wt % H_2O_2 aqueous solution at 80 °C for 1 h, then washed with ultrapure water until the pH value of the water returned to neutral, followed by boiling with dilute H_2SO_4 (5 wt%) at 80 °C for 1 h. Finally, the membrane was soaked with ultrapure water for 4 h. The electrochemical experiments were carried out with an electrochemical workstation (CHI 760E) using a three-electrode system with prepared NHCSs-carbon paper (NHCSs/CP, 0.05 mg cm^{-2}) electrode, Pt plate and Hg/HgO electrode as the working electrode, counter electrode and reference electrode, respectively.

To quantify the H_2O_2 produced, the samples were collected at certain time and mixed with same volume of $Ce(SO_4)_2$ solution (0.1 mmol L^{-1}). The H_2O_2 yield was measured by using the indicator of $Ce(SO_4)_2$ ($2Ce^{4+} + H_2O_2 \rightarrow 2Ce^{3+} + 2H+ + O_2$). The generated complex compound solution was detected with UV-vis spectrophotometer. A typical concentration-absorbance curve was calibrated by linear fitting the absorbance values at wavelength length of 320 nm for various known concentration of 0.02, 0.04, 0.06, 0.08, 0.1 mM of Ce^{4+}. The fitting curve (y = 0.4.8525x - 0.06965, R^2 = 0.99918) shows good linear relation of absorbance value with H_2O_2 concentration. The yield of H_2O_2 was finally determined based on the reduced Ce^{4+} concentration. The

FE for H_2O_2 generation in H-cell was calculated as follows:

$$FE\% = \frac{mole\ of\ generation\ H_2O_2 \times 2 \times 96485}{total\ consumed\ charge\ (C)}$$

The electrochemical impedance spectroscopy (EIS) was conducted from 100,000 to 1 Hz to determine the uncompensated resistance (Ru) in a high-frequency range for iR-correction.

Computational Methods: The spin-polarized density functional theory (DFT) calculations were performed with Vienna ab initio simulation package (VASP).[1] The interactions between the valence electrons and the ion cores were described by the projected augment wave (PAW) pseudopotential[2] and the exchange-correlation effects by the Perdew, Burke, and Ernzerhof (PBE) functional.[3] The van der Waals (vdW) interaction was included by using the DFT-D3 method.[4] The plane-wave basis was used with a kinetic energy cutoff of 450 eV. The convergence criteria for the total energy and the Hellmann-Feynman force are 10^{-5} eV and 0.02 eVÅ^{-1}, respectively. To consider the edge effect, two typical graphene nanoribbons have been adopted: the armchair (A) and zigzag (Z) graphene nanoribbons, with the ribbon widths of ~ 14 Å, respectively, as shown in Fig. S15. The COOH functionalized graphene nanoribbons were constructed by replacing an edge H atom with COOH group. In addition, we considered three types N atoms doping in the graphene nanoribbons, i.e., pyrrole N in Figure 4(a)/(d), pyridine N in Figure 4(b)/(e), and graphite N in Figure 4(c)/(f). For all the models, the vacuum layers were set to be 20 Å, to avoid the interaction between slabs. The Brillouin zone was sampled using the Monkhorst-Pack grids[5] of (1×3×1) and (2×1×1), respectively, for armchair and zigzag graphene nanoribbons.

The binding strength for the OOH* (ΔG_{HOO*}) is considered to be the best descriptor to evaluate the activity of 2e$^-$ ORR.[6-9] For the calculation of ΔG_{OOH*}, we have adopted the computational hydrogen electrode (CHE) model,[10] using the equation: $\Delta G = \Delta E + \Delta E_{ZPE} - T\Delta S$, where E, E_{ZPE}, and S denotes the total electronic energy, zero-point energy, and entropy of the relevant systems, respectively, and T is taken as 298.15 K. E_{ZPE} and S of the adsorbed intermediates were obtained from DFT calculations, while those of the free molecules (H_2 and H_2O) taken from the NIST databases.[11] It is

noted that the solvation effect may bring a small stabilization on the adsorbed OOH, while the reported activity trend should keep unchanged without the solvation correction. In fact, although in the previous works on the 2e[-] ORR[6-9] DFT calculations did not consider the solvation effect, the good agreement between the experimental and theoretical results were observed. Therefore, as previous works,[6-9] herein we did not consider the solvation effect in determining the value of ΔG_{OOH*}, which in turn allows us to make a direct comparison with the previous results.[6-9] The limiting potential (U_L) is defined as the maximum potential at which all the reaction steps are downhill in the free energy, and the theoretical overpotential as the difference between the thermodynamic equilibrium potential and the limiting potential.

An active catalyst for 2e[-] ORR to H_2O_2 should have a sizable limiting potential close to the equilibrium potential (0.70 V vs SHE). The ideal situation is that the Gibbs free energy changes in each elementary step are the same at zero potential so that all reaction free energies are zero when the electrode potential reaches the equilibrium potential. Consequently, the optimal ΔG_{OOH*} value is estimated to be 4.22 eV.
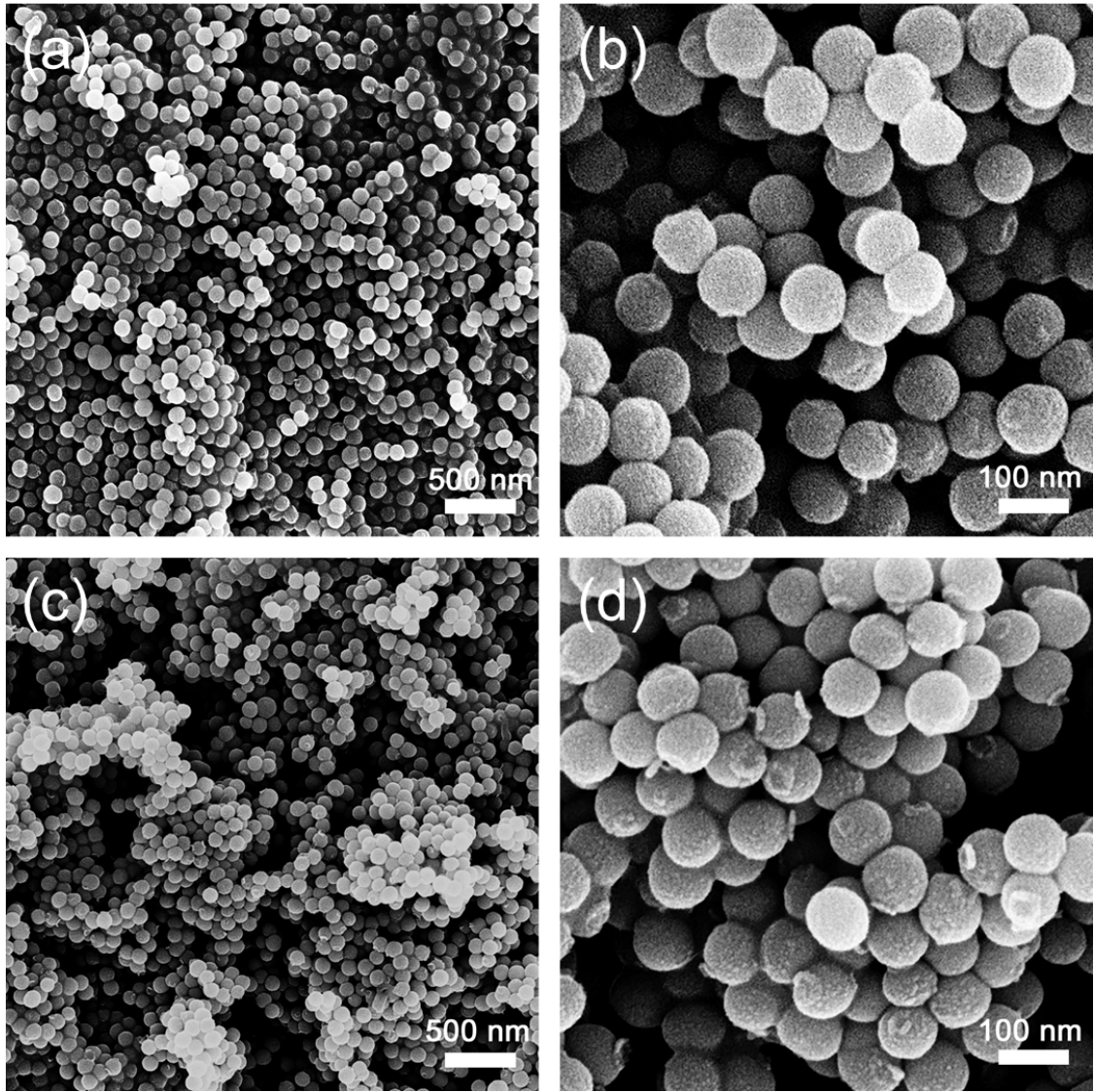
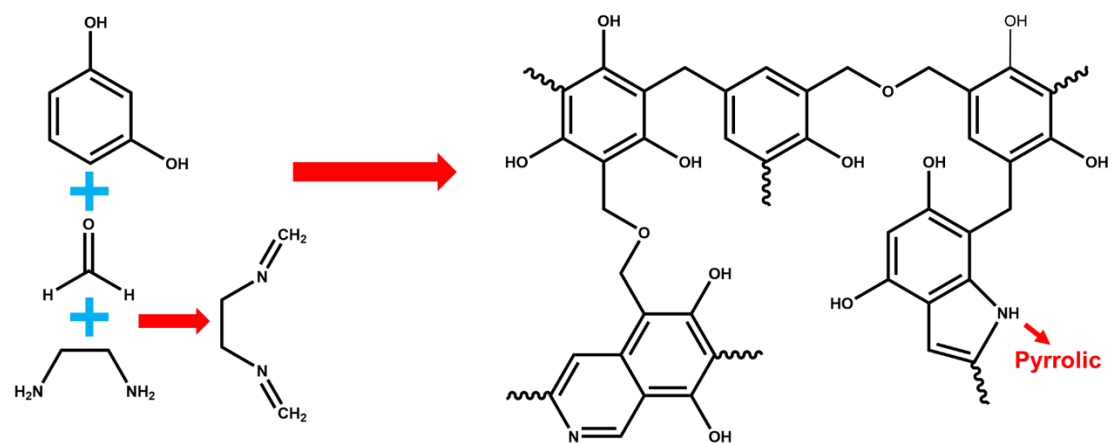**Fig. S1.** SEM images of SiO$_2$@N containing polymer layers before (a, b) and after (c, d) pyrolysis.

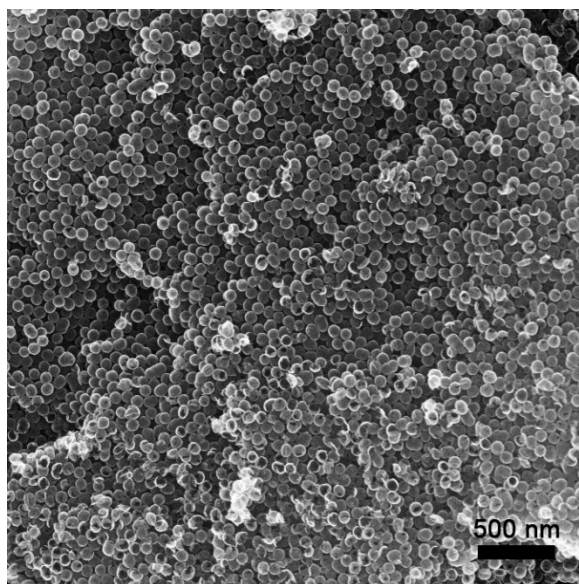**Fig. S2.** Representation of possible resorcinol−formaldehyde−ethylenediamine Polymerization.
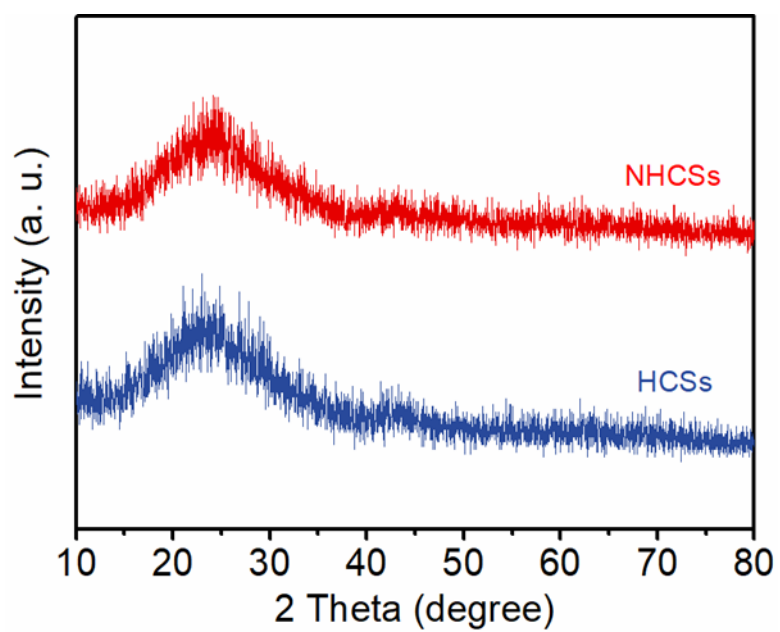
Fig. S3. SEM image of NHCSs
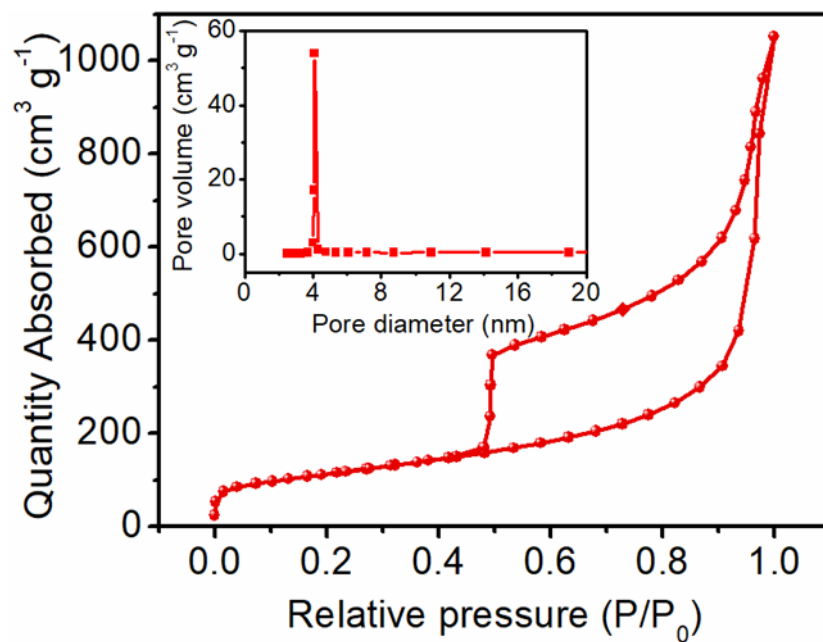
Fig. S4. XRD patterns of NHCSs and HCSs.

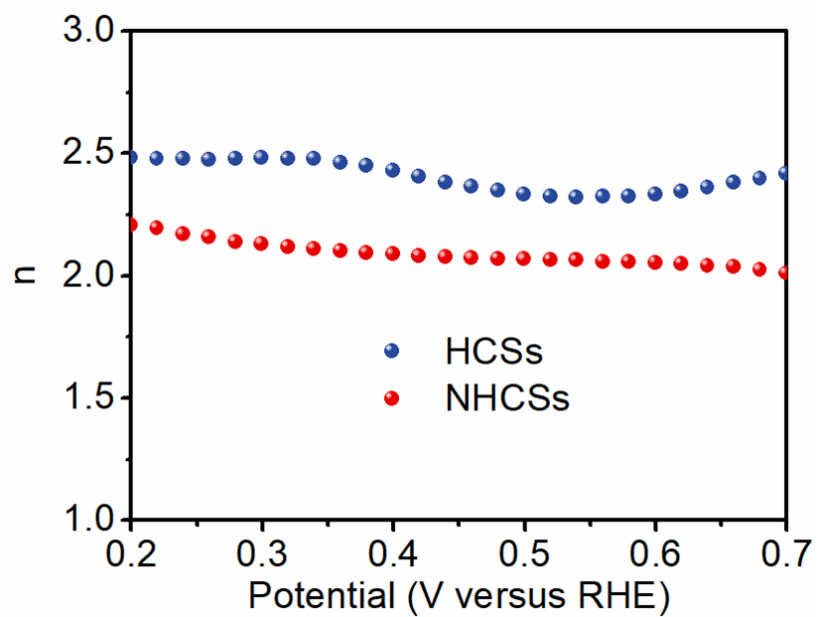**Fig. S5.** N$_2$ sorption isotherms of HNCSs and corresponding pore size distribution plots (The inset).

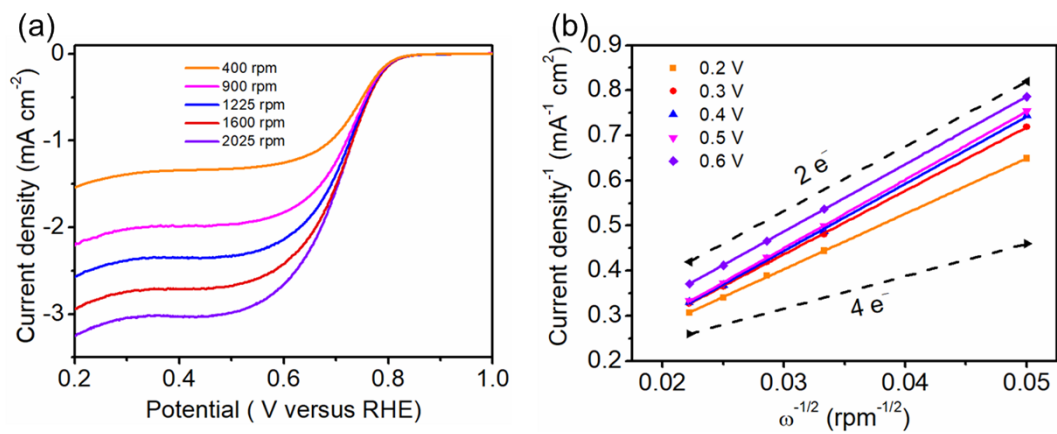**Fig. S6.** Calculated electron transfer numbers of HCSs and NHCSs.

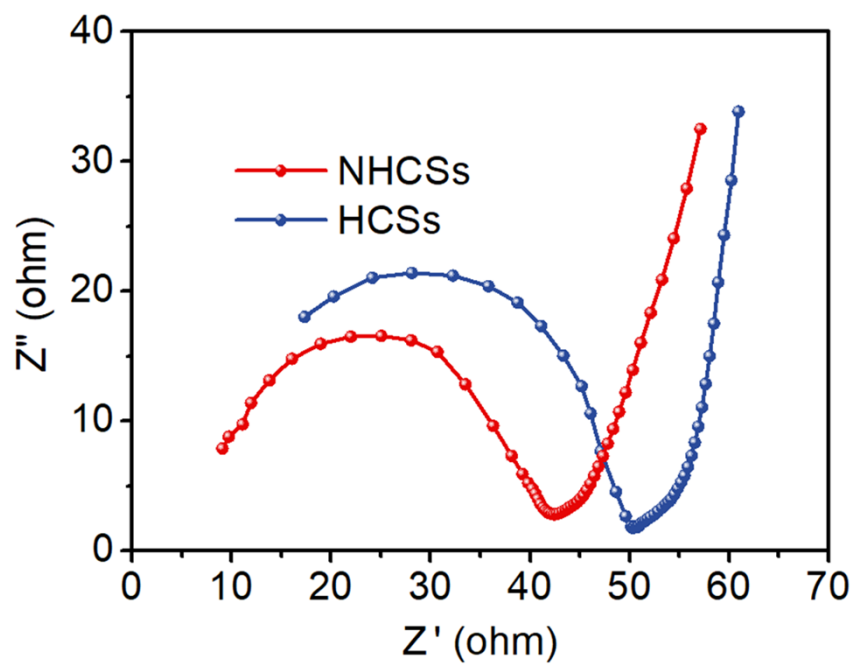**Fig. S7.** (a) LSV curves of NHCSs at different rotation rates and (b) corresponding Koutecky-Levich (K-L) plots.

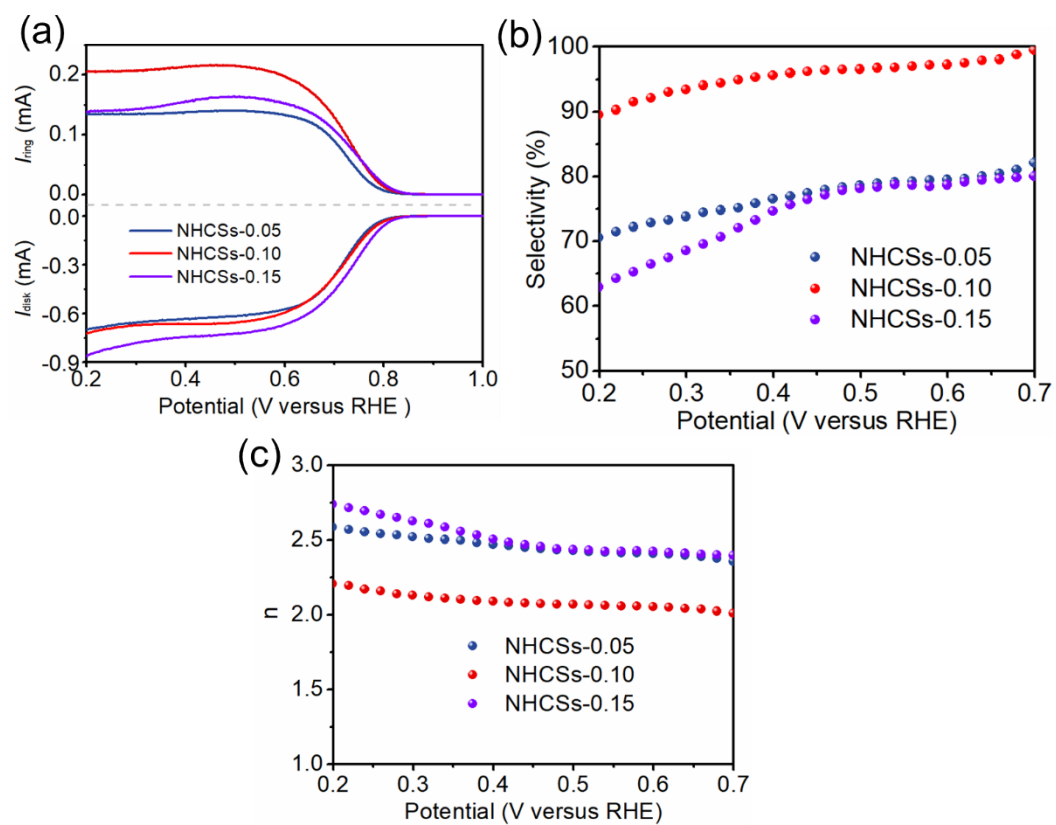**Fig. S8**. The EIS plots of NHCSs and HCSs on RRDE.

Fig. S9. (a) Polarization curves of NHCSs with different concentrations of N doping. (b) Calculated selectivity. (c) Corresponding electron transfer numbers.
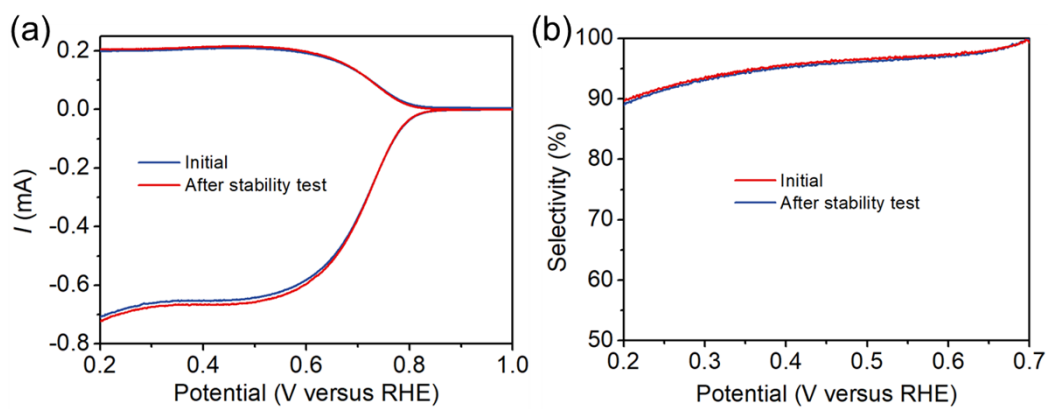
Fig. S10. RRDE curves (a) and calculated selectivity (b) before and after 12 h stability test.
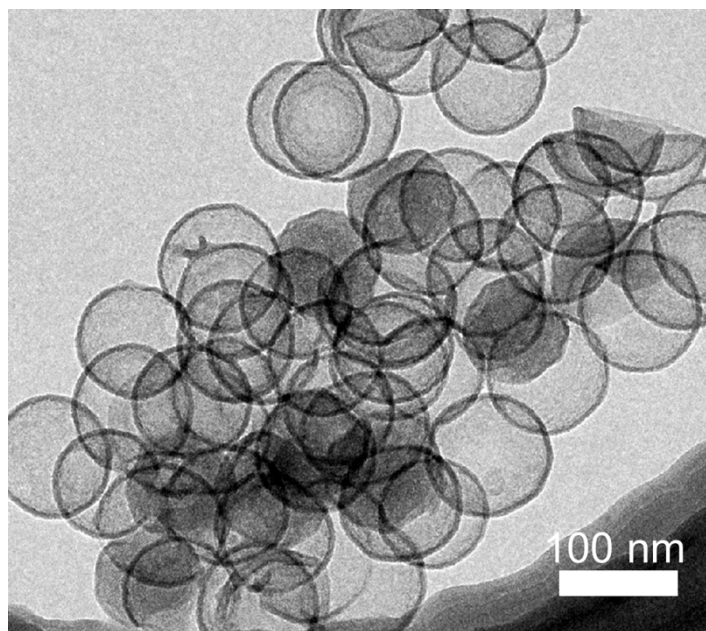
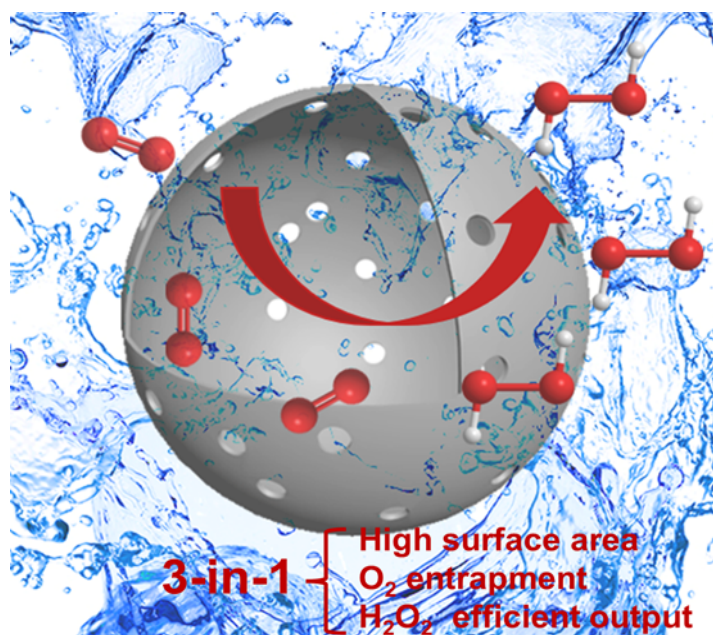**Fig. S11.** TEM image of NHCSs after long-term RRDE electrolysis.

Fig. S12. The 3-in-1 effect of NHCSs facilitates O_2-to-H_2O_2 conversion.

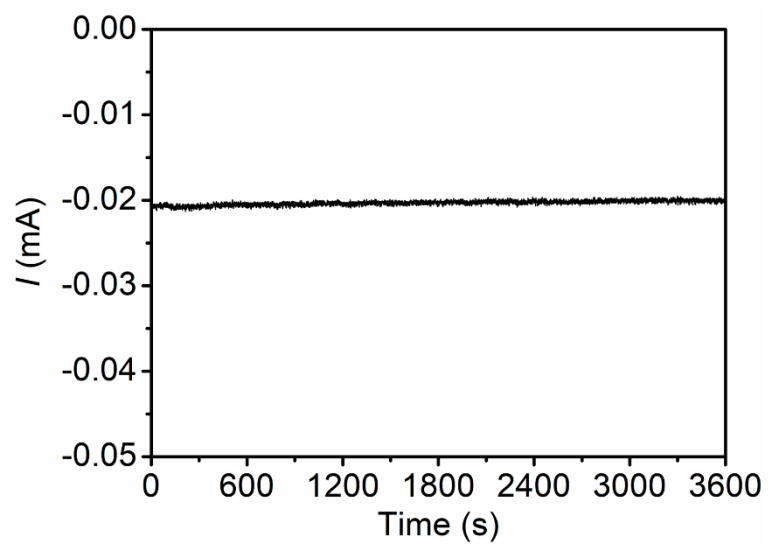**Fig. S13.** Time-dependent current curve of NHCSs in O_2-saturated 0.1 M KOH at 0.5 V.
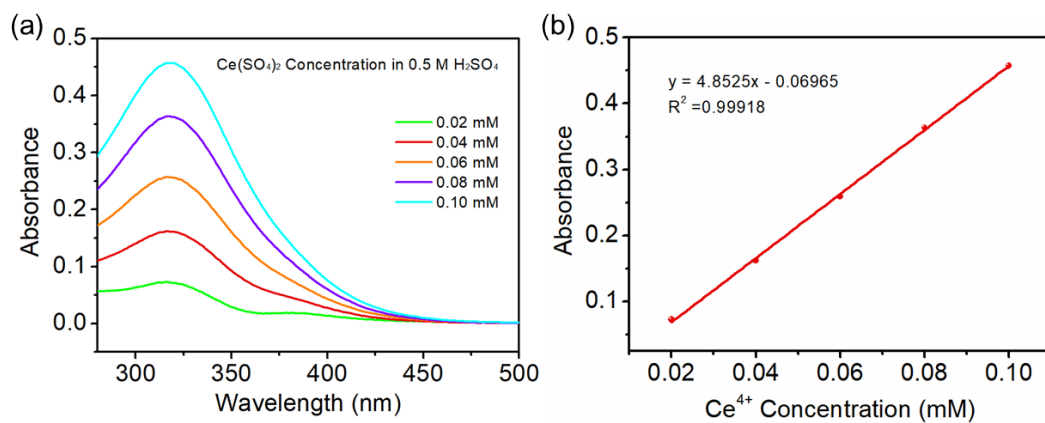
Fig. S14. (a) UV-Vis spectra of Ce^{4+} solution with various concentrations and (b) corresponding standard curve.
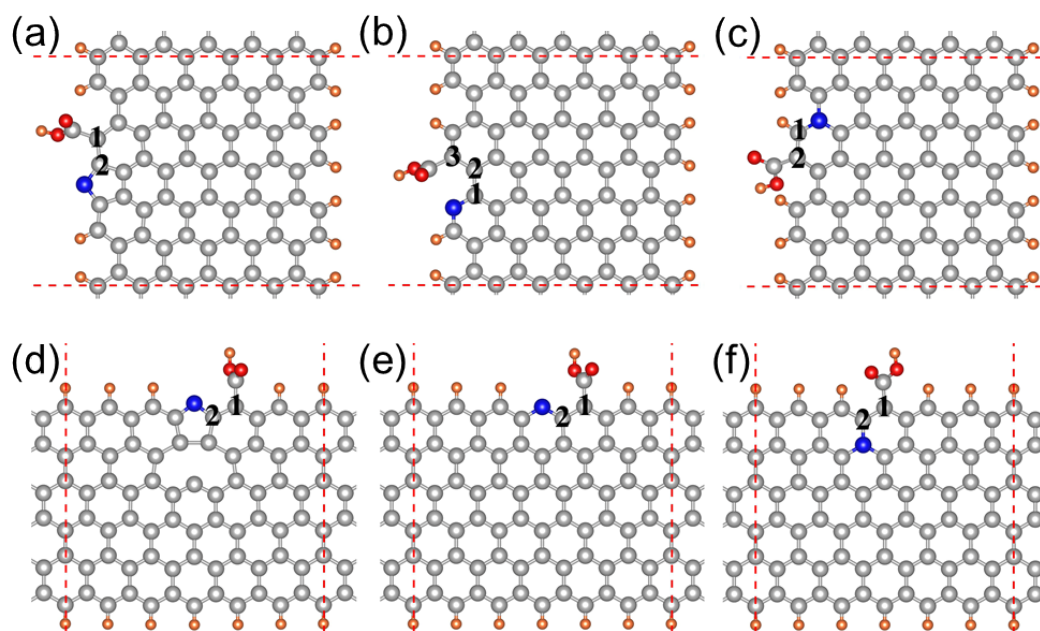
Fig. S15. Optimized configurations of COOH group modified graphene nanoribbons with N doping at armchair/zigzag edges in pyrrole type (a)/(d), pyridine type (b)/(e), and graphite type (c)/(f).

Fig. S16. Optimized configurations of OOH intermediates adsorption at different edge sites on N doped and COOH radical modified graphene nanoribbons.

Fig. S17. Optimized configurations of OOH intermediates adsorption at different edge sites on COOH modified graphene nanoribbons. The black values are the corresponding limiting potentials.

Fig. S18. Optimized configurations of OOH intermediates adsorption at different edge sites on pristine graphene nanoribbons. The black values are the corresponding limiting potentials.

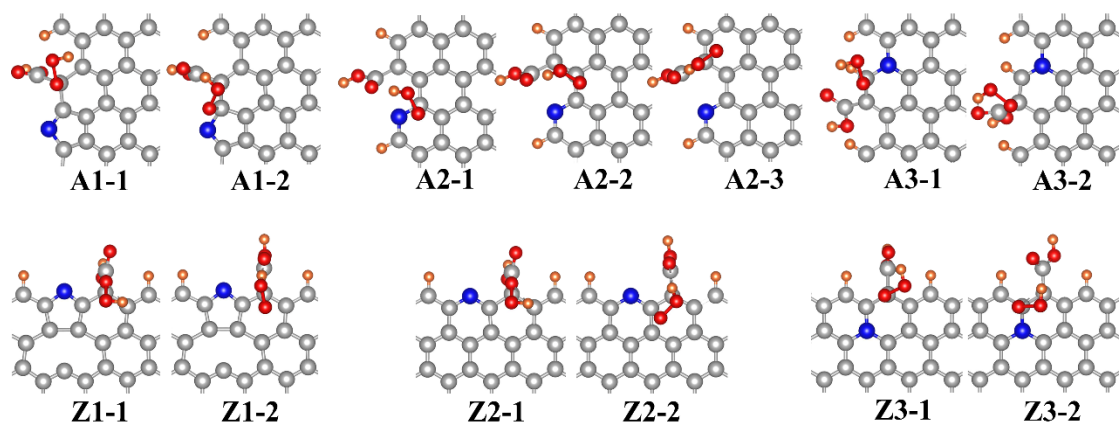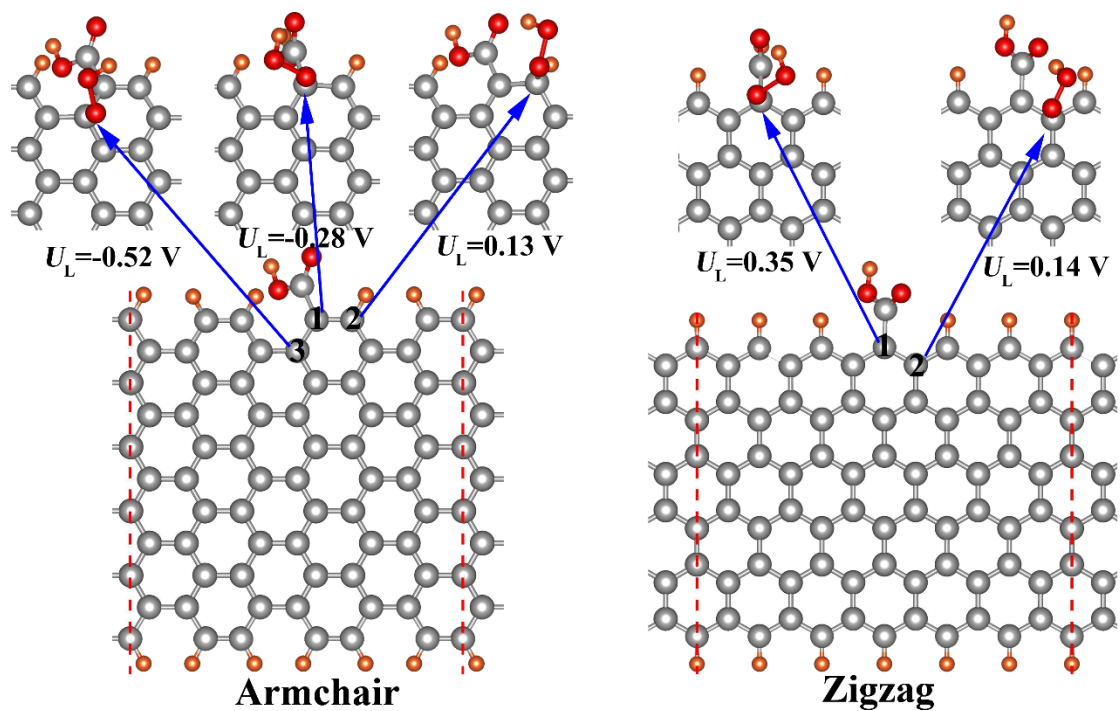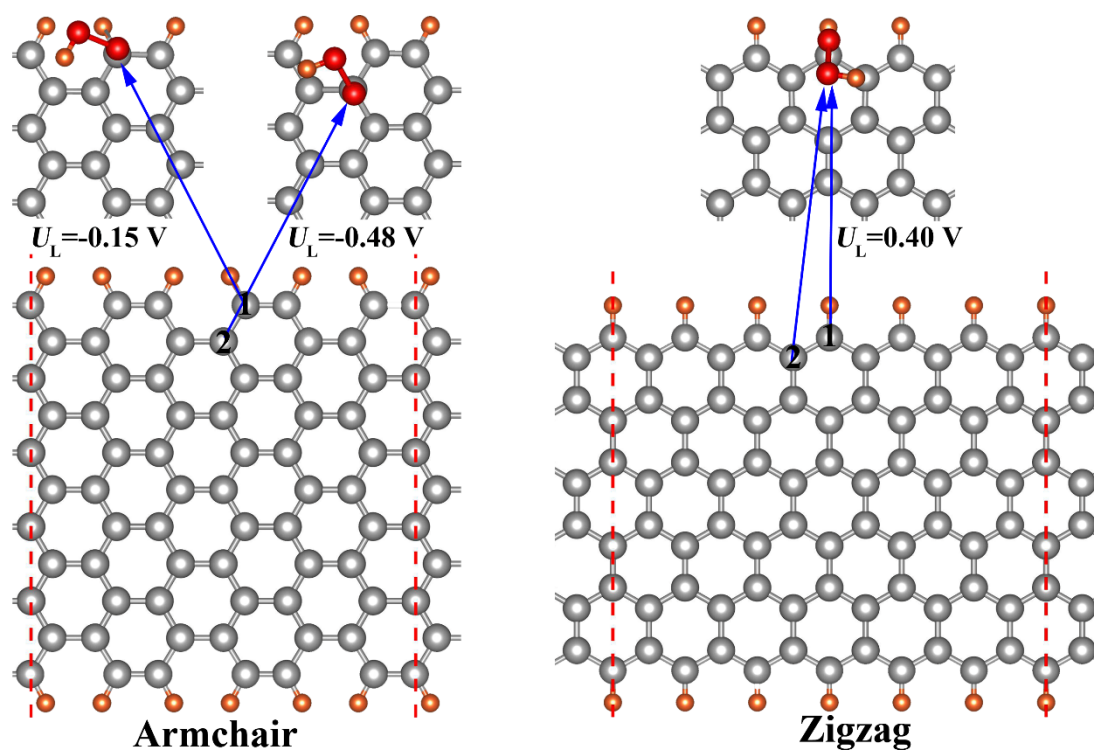**Table S1.** Comparison of the catalytic performance of NHCSs with reported 2e$^-$ ORR catalysts in alkaline media.

Electrocatalyst	Electrolyte	Selectivity [%]	Onset potential V vs. RHE	Reference
NHCSs	**0.1 M KOH**	**96.6**	**~0.82**	**This work**
O-CNTs	0.1 M KOH	90	0.8	7
Bi$_2$Te$_3$ NPs	0.1 M KOH	100	~0.75	12
Co1-NG(O)	0.1 M KOH	82	0.8V	13
N-FLG-8	0.1 M KOH	95	0.8	14
Co-POC-O	0.1 M KOH	84	0.79	15
MOF NSs-300	0.1 M KOH	99	0.75	16
Co-N-C	0.1 M KOH	~60	~0.82	17
Mo$_1$/OSG-H	0.1 M KOH	95	0.8	18
F-mrGO (600)	0.1 M KOH	100	0.7	19
BN-C1	0.1 M KOH	90	0.8	20
GO/H$_2$O$_2$/NH$_3$·H$_2$O	0.1 M KOH	82	0.76	21
HPCS-S	0.1 M KOH	70	/	22
rGO/PEI	0.1 M KOH	90.7	0.8	23
G-COF-950	0.1 M KOH	75	0.74	24
Ni-N$_2$O$_2$/C	0.1 M KOH	96	/	25
CMK3-20	0.1 M KOH	90	0.79	26
HCNFs	0.1 M KOH	97.3	0.80	27
OCNS$_{900}$	0.1 M KOH	90	0.825	28
CB-Plasma	0.1 M KOH	~100	0.80	29

Table S2. Calculated H_2O_2 productivity of NHCSs with reported $2e^-$ ORR catalysts using H-cell.

Electrocatalyst	Electrolyte	FE (%)	Productivity	Reference
NHCSs	**0.1 M KOH**	**96.7**	**7.32 mol $g_{cat}^{-1} h^{-1}$**	**This work**
Bi_2Te_3 NPs	0.1 M KOH	/	6.86 mmol $L^{-1} h^{-1}$	12
Co1-NG(O)	0.1 M KOH	/	~418 mmol $g^{-1} h^{-1}$	13
N-FLG-8	0.1 M KOH	~100	~9.66 mol $g_{cat}^{-1} h^{-1}$	14
Co-POC-O	0.1 M KOH	78	813 mg $L^{-1} h^{-1}$	15
MOF NSs-300	0.1 M KOH	N/A	~6.5 mol $g_{cat}^{-1} h^{-1}$	16
Co-N-C	0.1 M KOH	N/A	~4.33 mol $g_{cat}^{-1} h^{-1}$	17
$GO/H_2O_2/NH_3 \cdot H_2O$	0.1 M KOH	43.6	0.2248 mol $g_{cat}^{-1} h^{-1}$	21
HPCS-S	0.1 M KOH	70	0.184 mol $g_{cat}^{-1} h^{-1}$	22
rGO/PEI	0.1 M KOH	90.7	0.106 mol $g_{cat}^{-1} h^{-1}$	23
G-COF-950	0.1 M KOH	69.8	1.287 mol $g_{cat}^{-1} h^{-1}$	24
$Ni-N_2O_2/C$	0.1 M KOH	91	5.9 mol $g_{cat}^{-1} h^{-1}$	25
CMK3-20	0.1 M KOH	95	2.476 mol $g_{cat}^{-1} h^{-1}$	26
HCNFs	0.1 M KOH	/	6.37 mmol $L^{-1} h^{-1}$	27
$OCNS_{900}$	0.1 M KOH	89.6	770 mmol $g^{-1} h^{-1}$	28
CB-Plasma	0.1 M KOH	100	/	29

References

1. G. Kresse and J. Furthmüller, *Phys. Rev. B*, 1996, **54**, 11169.

2. P. E. Blöchl, *Phys. Rev. B*, 1994, **50**, 17953-17979.

3. J. P. Perdew, K. Burke and M. Ernzerhof, *Phys. Rev. Lett.*, 1996, **77**, 3865−3868.

4. S. Grimme, J. Antony, S. Ehrlich and H. Krieg, *J. Chem. Phys.*, 2010, **132**, 154104.

5. H. J. Monkhorst and J. D. Pack, *Phys. Rev. B*, 1976, **13**, 5188-5192.

6. S. Siahrostami, A. Verdaguer-Casadevall, M. Karamad, D. Deiana, P. Malacrida, B. Wickman, M. Escudero-Escribano, E. A. Paoli, R. Frydendal, T. W. Hansen, I. Chorkendorff, I. E. L. Stephens and J. Rossmeisl, *Nat. Mater.*, 2013, **12**, 1137-1143.

7. Z. Lu, G. Chen, S. Siahrostami, Z. Chen, K. Liu, J. Xie, L. Liao, T. Wu, D. Lin, Y. Liu, T. F. Jaramillo, J. K. Nørskov and Y. Cui, *Nat. Catal.*, 2018, **1**, 156–162.

8. X. Zhao, Y. Wang, Y. Da, X. Wang, T. Wang, M. Xu, X. He, W. Zhou, Y. Li, J. N. Coleman and Y. Li, *Natl. Sci. Rev.*, 2020, **7**, 1360-1366.

9. G. Han, F. Li, W. Zou, M. Karamad, J-P. Jeon, S-W Kim, S-J. Kim, Y. Bu, Z. Fu, Y. Lu, S. Siahrostami and J-B Baek, *Nat. Commun.*, 2020, **11**, 2209.

10. J. K. Nørskov, J. Rossmeisl, A. Logadottir, L. Lindqvist, J. R. Kitchin, T. Bligaard and H. Jónsson, *J. Phys. Chem. B*, 2004, **108**, 17886-17892.

11. http://webbook.nist.gov/chemistry/.

12. N. Zhang, F. Zheng, B. Huang, Y. Ji, Q. Shao, Y. Li, X. Xiao and X. Huang, *Adv. Mater.*, 2020, **32**, 1906477.

13. E. Jung, H. Shin, B.-H. Lee, V. Efremov, S. Lee, H. S. Lee, J. Kim, W. H. Antink, S. Park, K.-S. Lee, S.-P. Cho, J. S. Yoo, Y.-E. Sung and T. Hyeon, *Nat. Mater.*, 2020, **19**, 436–442.

14. L. Li, C. Tang, Y. Zheng, B. Xia, X. Zhou, H. Xu and S.-Z. Qiao, *Adv. Energy Mater.*, 2020, **10**, 2000789.

15. B.-Q. Li, C.-X. Zhao, J.-N. Liu and Q. Zhang, *Adv. Mater.*, 2019, **31**, 1808173.

16. M. Wang, N. Zhang, Y. Feng, Z. Hu, Q. Shao and X. Huang, *Angew. Chem. Int. Ed.*, 2020, **59**, 14373−14377.

17. Y. Sun, A. Bagger, N. Ranjbar, W. Ju, J. Li, A. Zitolo, S. Li, L. Silvioli, L.

Arnarson, X. Wang, T. Möller, D. Bernsmeier, J. Rossmeisl, F. Jaouen and P. Strasser, *J. Am. Chem. Soc.*, 2019, **141**, 12372–12381.

18. C. Tang, Y. Jiao, B. Shi, J. Liu, Z. Xie, X. Chen, Q. Zhang and S. Qiao, *Angew. Chem. Int. Ed*., 2020, **59**, 9171–9176.

19. H. W. Kim, M. B. Ross, N. Kornienko, L. Zhang, J. Guo, P. Yang and B. D. McCloskey, *Nat. Catal*., 2018, **1**, 282–290.

20. S. Chen, Z. Chen, S. Siahrostami, D. Higgins, D. Nordlund, D. Sokaras, T. R. Kim, Y. Liu, X. Yan, E. Nilsson, R. Sinclair, J. K. Nørskov, T. F. Jaramillo and Z. Bao, *J. Am. Chem. Soc*., 2018, **140**, 7851–7859.

21. L. Han, Y. Sun, S. Li, C. Cheng, C. E. Halbig, P. Feicht, J. L. Hübner, P. Strasser and S. Eigler, *ACS Catal*., 2019, **9**, 1283–1288

22. G. Chen, J. Liu, Q. Li, P. Guan, X. Yu, L. Xing, J. Zhang and R. Che, *Nano Res*., 2019, **12**, 2614–2622.

23. X. Xiao, T. Wang, J. Bai, F. Li, T. Ma and Y. Chen, *ACS Appl. Mater. Interfaces*, 2018, **10**, 42534–42541.

24. J. Zhang, G. Zhang, S. Jin, Y. Zhou, Q. Jia, H. Lan, H. Liu and J. Qu, *Carbon*, 2020, **163**, 154–161.

25. Y. Wang, R. Shi, L. Shang, G. I. N. Waterhouse, J. Zhao, Q. Zhang, L. Gu and T. Zhang, *Angew. Chem. Int. Ed*., 2020, **59**, 13057–13062.

26. Y. Wang, S. Li, X. Yang, G. Xu, Z. Zhu, P. Chen and S. Li, *J. Mater. Chem. A*, 2019, **7**, 21329–21337.

27. K. Dong, J. Liang, Y. Wang, Z. Xu, Q. Liu, Y. Luo, T. Li, L. Li, X. Shi, A. Asiri, Q. Li, D. Ma and X. Sun, *Angew. Chem. Int. Ed*., 2021, **60**, 10583–10587.

28. S. Chen, T. Luo, K. Chen, Y. Lin, J. Fu, K. Liu, C. Cai, Q. Wang, H. Li, X. Li, J. Hu, H. Li, M. Zhu and M. Liu, *Angew. Chem. Int. Ed*., 2021, **60**, 16607-16614.

29. Z. Wang, K. Li, C. Zhang, Z. Cheng, W. Chen, E. Mchugh, R. Carter, B. Yakobson and J. Tour, *ACS Catal*., 2021, **11**, 2454−2459.